

EPRI Task ID: 1-110095-01-04

**Early Stage Fatigue Damage Detection in Martensitic Steels Using
Nondestructive Electrical Birefringence Measurements**

Ethan Robinson and Peter B. Nagy

Department of Aerospace Engineering and Engineering Mechanics

University of Cincinnati

Cincinnati, Ohio 45221

submitted to

Electric Power Research Institute

1300 West WT Harris Blvd.

Charlotte NC 28262-7097

December 10, 2019

Summary

The objective of this project was to assess various Electromagnetic Nondestructive Evaluation (EMNDE) techniques that might be exploited for early detection and characterization of high-cycle fatigue damage in martensitic stainless steel with the ultimate goal of adaptation to field inspection of actual steam turbine blades. Thirty-six plane bending fatigue specimens representing various levels of high-cycle fatigue exposure were provided by EPRI for this study. These specimens were tested for the presence of fatigue-induced anisotropic texture by two directional electromagnetic NDE methods, namely low-frequency alternating potential drop (ACPD) inspection at 4 Hz and high-frequency eddy current (EC) inspection at 30 kHz and 500 kHz. It was found that ACPD measurements were strongly influenced by a positive geometrical anisotropy A_{shape} and by a much weaker also positive intrinsic anisotropy A_{intact} of the damage-free material, while the damage-induced anisotropy A_{damage} caused by fatigue cycling was negative and its magnitude increased with the number of fatigue cycles. In order to achieve higher sensitivity to near-surface crack precursors in high-cycle bending fatigue specimens, directional EC techniques were also investigated at 30 kHz and 500 kHz. These measurements were found to be much less sensitive to edge effects than low-frequency ACPD measurements and offered better sensitivity to bending fatigue because of their much smaller penetration depth controlled by the inspection frequency. In addition, EC anisotropy is a combination of resistivity and permeability effects, which makes it possible to optimize the sensitivity and selectivity of the inspection technique. While both 4-Hz ACPD and 30-kHz EC directional measurements exhibited some sensitivity to fatigue precursors, EC measurements conducted at 500 kHz showed the most promise for detection and quantitative assessment of crack precursors in fatigue damaged martensitic steel. Finally, nondirectional magnetic measurements were also conducted on the same specimens at 1.8 kHz to determine whether the magnetic permeability (MP) of the material was affected by fatigue cycling. It was found that high-frequency eddy current anisotropy correlates reasonably well ($R^2 = 0.82$) with nondirectional MP measurements that could be exploited to further increase both the sensitivity and selectivity of this method via a dual-mode inspection technique that could be realized with a single broadband directional probe coil using dual-frequency operation.

1. Introduction

Identification of potential NDE candidates for preventing unexpected turbine blade failures in the power generation industry continues to be of major interest to EPRI [1]. The ultimate goal of research in this area is detection and quantitative assessment of crack precursors before preexisting manufacturing defects or earlier nucleated service-related cracks reach the detectability threshold of state-of-the-art nondestructive inspection techniques. The presence of material damage might significantly reduce the time needed for a crack to grow from an undetectable size at one inspection to a critical size before the next inspection opportunity. It is widely recognized that most of the service life of a fracture critical component might very well be spent before crack initiation when early fatigue damage accumulation can be assessed only by sensitive and selective detection of subtle crack precursors. NDE techniques capable of detecting material damage at this level would allow increasing both the service life and operational safety of critical infrastructure. Towards this goal, the main objective of this project was to assess various electromagnetic NDE techniques that might be exploited for early detection and characterization of high-cycle fatigue damage in martensitic stainless steels with emphasis on those that might be ultimately suitable for field inspection of turbine blades used in power generation.

This report summarizes the results of a series of tests conducted in the NDE Laboratory operated in the Department of Aerospace Engineering and Engineering Mechanics of the University of Cincinnati to establish the feasibility of electromagnetic anisotropy measurements for the detection and quantitative assessment of high-cycle fatigue precursors in martensitic steels. Ultrasonic shear wave birefringence measurements are widely used for measuring the degree of acoustic anisotropy caused by a combination of crystallographic and morphological texture. The former is due to the elastic anisotropy of single crystals that leads to macroscopic anisotropy in polycrystalline materials with preferred grain orientation, while the latter is caused by other directional features, such as, preferentially oriented boundaries of elongated grains, precipitates, segregations, and micro cavities along those preferentially oriented grain boundaries, as well as dislocation networks and slip bands formed by directional fatigue stresses, etc. Unfortunately, the damage induced ultrasonic anisotropy is usually rather weak compared to the intrinsic crystallographic texture of the material to be tested. In contrast, electrical conductivity, which is a second-order tensor versus the fourth-order elastic stiffness tensor, is

completely isotropic in cubic crystals, i.e., in the overwhelming majority of metal alloys of engineering interest [2]. Therefore, the electrical anisotropy is very sensitive to subtle morphological anisotropy caused by service-related directional effects, such as, uniaxial elastic stress, plastic deformation, creep damage and fatigue damage [3-6].

It should be emphasized that electrical measurements are neither the most sensitive nor the most selective NDE methods available for early fatigue damage detection; that distinction belongs to nonlinear ultrasonic methods that are uniquely sensitive to increasing dislocation size and density [7]. However, nonlinear ultrasonic techniques are mostly limited to laboratory environment and far more difficult to adapt to field inspection than most other NDE methods, while the long-term goal of this effort is to identify the most promising candidates for field inspection of actual steam turbine blades. In contrast, electric measurements are much less sensitive and selective to increasing dislocation size and density at room temperature when the lack of lattice periodicity is mainly due to thermal vibrations. This inherent disadvantage of electric NDE methods compared to nonlinear ultrasonic ones vanishes only at very low temperatures when the residual resistivity of metals depends on impurities and other crystallographic defects rather than temperature. However, EMNDE methods are far more adaptable to field inspection, therefore they certainly deserve a fair comparison in a multidisciplinary feasibility study like this one. To suppress the adverse effect of the isotropic “high-temperature” component of the electrical resistivity that dominate over the residual resistivity of the material even at room temperature, this project focused on relative anisotropy measurements using directional EMNDE methods that are expected to be more closely related to fatigue-induced crystallographic defects than traditional nondirectional absolute measurements.

Table 1 lists the martensitic steel specimens provided by EPRI for this study. The complete inventory consisted of thirty-six specimens subjected to different numbers of bending cycles to induce fatigue and contained some “new” intact specimens without any fatigue damage as well as “spent” specimens with initiated cracks. Figure 1 shows the geometry of the plane bending fatigue specimens provided by EPRI with the dimensions in inches unless otherwise noted. Figure 1 also shows the ten inspection locations selected in the gage section along the center line of the specimen. Because of the rather limited spatial resolution of the electrical anisotropy measurement techniques used in this study, the measurement locations were separated from each other by 1”. The specimens have tapered gauge sections subjected to uniform stress. Figure 2 shows the expected stress distribution on bending specimens obtained by finite element

Table 1 List of the thirty-six high-cycle martensitic steel specimens inspected in this study.

#	Specimen ID	Cycles	Stress (ksi)	Set	Note
1	41C	0	88	S1	
2	43C	0	88	S1	
3	44C	0	88	S2	
4	45C	0	88	S2	
5	7C	150,000	88	S1	
6	13C	150,000	88	S1	
7	8C	150,000	88	S2	
8	35C	150,000	88	S2	
9	24C	300,000	88	S1	
10	34C	300,000	88	S1	
11	9C	300,000	88	S2	
12	10C	300,000	88	S2	
13	19C	450,000	88	S1	
14	30C	450,000	88	S1	
15	32C	450,000	88	S2	
16	46C	450,000	88	S2	
17	23C	600,000	88	S1	
18	25C	600,000	88	S1	
19	21C	600,000	88	S2	
20	47C	600,000	88	S2	
21	27C	750,000	88	S1	
22	26C	750,000	88	S1	
23	28C	750,000	88	S2	
24	48C	750,000	88	S2	
25	37C	900,000	88	S1	
26	39C	900,000	88	S1	
27	42C	900,000	88	S2	
28	49C	900,000	88	S2	
29	20C	2,000,000	88	S1	
30	36C	348,957	88	S1	Cracked
31	6C	318,528	88	S2	Cracked
32	31C	1,073,548	88	S1	Cracked
33	29C	784,540	88	S2	Cracked
34	14C	2,000,000	84	S1	Different stress level
35	38C	2,000,000	84	S2	Different stress level
36	16C	2,000,000	80	S2	Different stress level

simulation [1]. This special shape was chosen so that regions in the gauge section away from any crack experience similar stress and likely exhibit similar levels of precursor damage, therefore provide indication of the material damage obtained near the fatigue life limit.

This project exploited the fact that at low frequencies the electrical anisotropy can be measured by directional, e.g., square-electrode four-point ACPD probes, while at higher frequencies it can be measured even more accurately by directional, e.g., elliptical, racetrack, meandering, etc., eddy current probe coils. First, the selected low-frequency ACPD measurement procedure will be described and the obtained ACPD results will be presented in Section 2. Similarly, Section 3 starts with a brief description of the high-frequency EC measurement procedure and then presents the ACPD results obtained at two different frequencies. Next, the experimental procedure used for magnetic permeability measurement will be presented in Section 4 followed by the obtained results in terms of relative magnetic permeability. Finally, Section 5 discusses the main findings of this study and summarizes the conclusions drawn from these results.

2. Alternating Current Potential Drop (ACPD) Measurements

The first EMNDE method used in this project to measure the electrical resistivity anisotropy of bending specimens relied on contact low-frequency ACPD measurements between 1 and 20 Hz. Compared to EC measurements, ACPD measurements offer deeper penetration depth albeit at the expense of lower detection sensitivity. At sufficiently low inspection frequencies the penetration depth is controlled by a combination of the electrode separation and specimen thickness, and the adverse influence of magnetic permeability variations can be effectively suppressed [8]. In addition to separating damage-induced conductivity variations from parallel magnetic permeability variations, this technique could also be used in the future to obtain estimates for the magnetic permeability variations by exploiting anisotropic magnetostriction to monitor changes caused by applied stress in steels [9].

2.1 ACPD Measurement Procedure

Directional ACPD measurements were conducted using a Stanford Research SIM921 AC resistance bridge with a $d = 10$ mm square electrode probe. In order to increase the sensitivity of the instrument, a four-fold Jensen JT-347 1:8 step-up transformer was used for impedance matching purposes. The deployable square-electrode ACPD probe consisted of four spring-loaded heavy-duty pins embedded in a Plexiglas fixture [10]. It should be mentioned that the

probe was manually rotated rather than electronically switched for texture measurements so that intrinsic geometrical errors due to variable pin positioning could be better suppressed.

Figure 3 shows the electrical resistance measured by this ACPD technique as a function of frequency in an intact specimen. The low-frequency asymptote is constant at $R_0 = 6.52 \mu\Omega$. At higher frequencies the measured impedance becomes complex as the injected current gets squeezed into the electromagnetic skin depth δ which is inversely proportional to frequency

$$\delta = \frac{1}{\sqrt{\pi f \mu_0 \mu_r \sigma_0}}, \quad (1)$$

where f denotes the inspection frequency, μ_0 is the magnetic permeability of free space, and μ_r and σ_0 are the relative permeability and electrical conductivity of the material, respectively. Due to the electromagnetic skin effect, the resistance, i.e., the real part of the frequency-dependent complex impedance, approaches its high-frequency asymptote that is proportional not only to the square root of the electrical resistivity $\rho_0 = 1/\sigma_0$, but also to the square root of the inspection frequency. The corner frequency f_c between these two regions is defined as the interception point of the low- and high-frequency asymptotes that can be numerically determined from the best fitting regression curve as described in [8]. For the square-electrode ACPD probe of $d = 10$ mm electrode separation used in this study, the corner frequency comes out to be $f_c = 17.2$ Hz. Generally, the corner frequency depends on the shape and size of the electrode configuration as well as the thickness ($t = 13.5$ mm) and material properties (μ_r and σ_0) of the specimen. Based on the magnetic permeability measurements to be presented in Section 4.2, the relative magnetic permeability of the martensitic steel specimens provided by EPRI for this study is $\mu_r \approx 180$. With these material properties, the standard penetration depth at the corner frequency is $\delta(f_c) \approx 7.5$ mm, i.e., lower than both the electrode separation d and the plate thickness t . In order to focus on electrical resistivity variations and avoid any influence by the more variable magnetic permeability, low-frequency ACPD measurements were conducted in this study at $f = 4$ Hz, i.e., well below the $f_c = 17.2$ Hz corner frequency.

Since the measured resistance is a rather complicated function of both plate thickness and probe geometry, absolute calibration of the ACPD resistance measurements required comparison to COMSOL Multiphysics finite element (FE) simulation. Based on the FE simulation results, the previously determined $R_0 = 6.52 \mu\Omega$ electrical resistance corresponds to $\rho_0 = 67.0 \mu\Omega\text{cm}$ electrical resistivity or $\sigma_0 = 1.49 \times 10^6$ S/m electrical conductivity, which is

$\sigma_0 = 2.58 \%$ IACS in terms of the International Annealed Copper Standard (IACS) preferred in eddy current inspection.

For the reasons described above, instead of absolute electrical resistance measurements, this study relied on relative electrical resistance anisotropy measurements conducted using a directional ACPD technique. The relative electrical resistance anisotropy A_R was calculated from the actually measured parallel R_{parallel} and normal R_{normal} resistances as follows

$$A_R = \frac{R_{\text{parallel}} - R_{\text{normal}}}{(R_{\text{parallel}} + R_{\text{normal}})/2}, \quad (2)$$

where the parallel and normal directions refer to the orientation of the injection electrode pair relative to the axis of the specimen. It should be pointed out that the thereby defined electrical resistance anisotropy is not only sensitive to the sought electrical resistivity anisotropy of the material, but also to geometrical effects, such as nearby edges of the specimen or cracks either between the electrodes under the probe or close to the electrodes outside the probe. In general, for relatively modest levels of anisotropy the following linear superposition suffices [4, 10]

$$A_R = A_{\text{shape}} + M A_{\text{material}}, \quad (3)$$

where A_{shape} is the baseline resistance anisotropy determined by the size and shape of the specimen compared to the probe dimensions, M is a gauge factor depending on the directionality of the probe, and the material anisotropy is defined as follows

$$A_{\text{material}} = \frac{\rho_{\text{parallel}} - \rho_{\text{normal}}}{(\rho_{\text{parallel}} + \rho_{\text{normal}})/2}, \quad (4)$$

where ρ_{parallel} and ρ_{normal} are the parallel and normal electrical resistances of the material under test relative to the axis of the specimen. The gauge factor M depends on the ratio between the electrode separation and the specimen thickness (d/t), but it is always between limits $M_{\text{thin}} \approx 1.4 \leq M \leq M_{\text{thick}} \approx 1.7$ that can be analytically calculated for very thin ($t \ll d$) and very thick ($t \gg d$) plates [4].

Unfortunately, for the relatively large $d = 10$ mm electrode separation A_{shape} turns out to be far from negligible even for the relatively large specimens used in this study. This is an inherent geometrical limitation of the directional ACPD technique that could be suppressed only by reducing the electrode separation. However, the spring-loaded electrodes used in such probes typically have a $\pm 50 \mu\text{m}$ targeting uncertainty that inherently limits the anisotropy measurements

when smaller probes are used. To illustrate this adverse effect, Figure 4 shows COMSOL Multiphysics FE simulation results obtained for the electric potential distribution on the actual specimen and probe geometries used in this study for both parallel and normal probe orientations relative to the axis of the specimen, which coincides with the uniaxial stress direction in the bending specimens during loading. It is clear that close to the narrow necking region of the gauge section the electric potential distribution is significantly affected by the closeness of the side edges of the specimen. Because of this distortion of the potential field, the transfer resistance measured by the four-point ACPD probe will be also affected. Figure 5 shows the parallel and normal resistances along the axis of the specimen obtained from the same FE simulation. As expected, both resistances peak in the necking region of the specimen, but the increase is significantly stronger for parallel probe orientation, i.e., when the injected current is parallel with the side edges of the specimen. Figure 6 shows the resulting geometrical anisotropy calculated using Eq. (2) along the axis of the specimen. For the given dimensions of the specimen and the ACPD probe, the resulting geometrical anisotropy A_{shape} can be as high as 10 %. Therefore, measurements taken too close to the necking at locations 9 and 10 will have to be discarded as unreliable due to small variations in the probe position.

Finally, it should be mentioned that the material anisotropy defined in Eq. (4) can be further divided into the sum of an intrinsic anisotropy part A_{intact} present even in the intact material and a damage induced part A_{damage} due to fatigue cycling

$$A_{\text{material}} = A_{\text{intact}} + A_{\text{damage}}. \quad (5)$$

The intrinsic anisotropy part A_{intact} is mainly due to morphological features, such as elongated grain shapes, but some crystallographic texture can also occur. As it was mentioned earlier, pure crystallites of cubic symmetry, such as fcc austenite and bcc ferrite, do not exhibit any crystallographic anisotropy in their electrical resistivity. However, even pure crystallites of tetragonal symmetry, such as bct martensite, exhibit crystallographic anisotropy in their electrical resistivity. However, in this limited study no attempt was made to separate these effects and the results will be presented in terms of the measured resistance anisotropy A_R as it was defined earlier in Eq. (2).

ACPD resistance measurements were taken at 4 Hz with both parallel and normal probe orientation at the ten locations specified in Figure 1. All measurements were repeated by five times to check repeatability and increase the overall accuracy by averaging. In most cases the

manually taken line scans exhibited significant point-to-point variation even after averaging the five values measured at the same location, therefore further spatial averaging was applied. The measured anisotropy values were averaged over locations 3-8 and 5-8. Two measurement locations on the left (1 and 2) and two on the right (9 and 10) were excluded from both spatial averages. The two locations on the left were excluded because the wide region of the gauge section close to the rigidly clamped end, in spite of the relatively uniform stress distribution predicted by FE simulations, exhibited systematically less fatigue damage than the other end. The two locations on the right were excluded because the narrow necking region of the gauge section close to the cyclically loaded end exhibited rather strong geometrical anisotropy that made the measurement too sensitive to probe positioning.

2.2 ACPD Measurement Results

Although low-frequency ACPD and high-frequency EC techniques were selected for inclusion in this study mainly because their potential for detecting precursors of fatigue damage before crack initiation, the same type of measurements were also conducted on the four cracked specimens (6C, 29C, 31C and 36C) listed in Table 1. In spite of the rather large 1" stepping size used during manual scanning of the specimens, ACPD inspection is capable of detecting such gross defects because of its high sensitivity and inherently low spatial resolution. Figure 7 shows the ACPD resistance anisotropy measured on four cracked specimens along their axes. All four specimens exhibited easily detectable anisotropy anomalies in the vicinity of the visually detectable fatigue cracks. In addition, all four specimen exhibited essentially the same geometrical anisotropy A_{shape} with a peak around 11% in the vicinity of the necking region of the gauge section as it was predicted by FE simulations in Figure 6.

One interesting feature of the results shown in Figure 7 is that the defect indication associated with the crack of specimen 31C exhibited a negative peak, while the other three defect signatures all exhibited positive peaks. The explanation for this difference lies in the different relative positions of the cracks present in these specimens relative to the arbitrarily defined measurement positions separated by 1" from each other. As an example, Figure 8 shows the optical images and schematic diagrams of cracked specimens 31C and 36C. In the case of Specimen 31C the transverse fatigue crack lies on the left of the ACPD probe centered on location 5, therefore the resistance measured at normal orientation R_{normal} increased more than

the resistance measured at parallel orientation R_{parallel} . As a result, the resistance anisotropy defined in Eq. (2) is negative. In contrast, in the case of Specimen 36C the transverse fatigue crack lies directly under the ACPD probe centered on location 7, therefore the resistance measured at parallel orientation R_{parallel} increased more than the resistance measured at normal orientation R_{normal} . As a result, the resistance anisotropy defined in Eq. (2) is positive. In the case of the other two cracked specimens (6C and 29C) the situation is similar to that of specimen 36C, therefore they also exhibit crack indications with positive peaks.

Of course the main objective of this study was to detect crack precursors in bending specimens exposed to high-cycle fatigue damage rather than large terminal cracks. Figure 9 shows the ACPD resistance anisotropy measured at 4 Hz as a function of the number of fatigue cycles in thirty-two uncracked specimens. All specimens, except for three cases ran to $N = 2 \times 10^6$ cycles, were loaded at $\tau = 88$ ksi peak stress level (see Table 1). The three exceptions included two specimens (14C and 38C) cycled at 84 ksi and one specimen (16C) cycled at 80 ksi. As explained in the previous section, two sets of data are presented. Open red and blue circles represent anisotropy values spatially averaged over locations 3-8 and 5-8, respectively, for four single specimens at each fatigue level. In addition, solid circles of the same color indicate the ensemble average for each group of four singles tested at the same stress level (see comments above for $N = 2 \times 10^6$ cycles). Finally, solid lines are trend lines intended to schematically illustrate overall trends in the data.

Both shorter (5-8) and longer (3-8) averages indicate the same decreasing trend with increasing cycle number. The difference in absolute values is due to the uncorrected geometrical anisotropy A_{shape} caused by the tapered width of the specimens (see Figure 6). As expected, the total resistance anisotropy is roughly 0.7% lower when the spatial averaging includes two additional locations (3 and 4) where A_{shape} is lower because those points are further away from the necking region. The fact that the measured total anisotropy decreases with increasing number of fatigue cycles indicates that the positive geometrical anisotropy A_{shape} , together with the much weaker also positive intrinsic anisotropy A_{intact} of the intact, i.e., damage-free, material is partially compensated by the increasing magnitude of the negative damage-induced anisotropy A_{damage} caused by fatigue cycling. However, the overall magnitude of A_{damage} is only about 1%. Because of the computationally determined $M \approx 1.5$ value of the above introduced anisotropy gauge factor [4], the damage induced change in the material anisotropy defined by Eq. (4) is only about 0.7%. It is likely that the actual material anisotropy caused by fatigue damage is

significantly higher in the thin surface layers of the specimen that are much more affected by bending fatigue than deeper regions close to the midplane of the specimens. Although low-frequency ACPD exhibits higher sensitivity to resistivity changes on the top surface where the probe is mounted than changes at the opposite bottom surface, this purely geometrical effect is insufficient for significant sensitivity enhancement in the most affected surface layers. Because of the inverse square root relation between electromagnetic skin depth and inspection frequency previously shown in Eq. (1), limiting the penetration depth of ACPD measurements in the type of ferromagnetic steels considered in this study would require rather high inspection frequencies. For example, $\delta = 1$ mm penetration depth is reached at around $f = 1$ kHz. Technically, ACPD measurements can be conducted in the kHz range, but complications arise because of the inherent inductive coupling between the injection and sensing loops that require special measures to suppress. Also, ACPD and other electromagnetic measurements at such high frequencies would become sensitive to not only resistivity anisotropy, but permeability anisotropy as well, which significantly increases the complexity of evaluating the measured results. Since high-frequency directional conductivity measurements are more easily achieved using EC techniques, as it will be shown in the next section, increasing the inspection frequency of ACPD measurements above the $f_c \approx 17$ Hz corner frequency of the current probe was not attempted in this limited feasibility study.

3. Eddy Current (EC) Measurements

In order to achieve higher near-surface sensitivity to damage-induced electrical conductivity anisotropy in the high-cycle fatigue specimens provided for this project by EPRI, directional EC techniques were also tested. Directional EC techniques are non-contact in nature, offer shallow penetration depth that can be easily controlled by changing the inspection frequency, and are sensitive to not only electrical anisotropy, but also magnetic anisotropy. Eddy current conductivity anisotropy measurements, often referred to as “birefringence” measurements, are made with directional, usually racetrack-shaped, eddy current probe coils that can be rotated on the surface like linearly polarized shear wave transducers are in ultrasonic birefringence measurements. Using custom-made probe coils of aspect ratio of 4 or higher, such conductivity anisotropy measurements can be made with better than 0.1% accuracy from a few hundred hertz

up to a few megahertz with a rugged and portable eddy current instrument like the Nortec 2000D used in this study.

In EC measurements, changing the inspection frequency allows easy control of the penetration depth to match the depth distribution of the fatigue damage produced by bending stresses that are strong at the surface but vanish at the neutral midplane of the bending specimen. For example, at $f = 30$ kHz inspection frequency the standard penetration in the martensitic steel specimens used in this study is only $\delta \approx 0.18$ mm, which is sufficiently small compared to the thickness $t = 13.5$ mm of the specimens to limit the inspection to the shallow surface layer most affected by bending stresses. In addition, EC measurements conducted along the axis of fairly large specimens are not sensitive to edge effects the way low-frequency ACPD measurements were. The reason for this is that the eddy current distribution induced in the specimen is essentially a mirror image of the driving current flowing in the probe coil, though, of course according to Lenz law, it is running in the opposite direction. The lateral spread of the eddy current distribution relative to the constrained channel presented by the probe coil is on the order of the standard penetration depth [11], which is negligible with respect to the size of the roughly 10 mm long and 2.5 mm wide racetrack probe coils used in this study. As a result, the geometrical anisotropy A_{shape} in Eq. (3), which in the case of ACPD measurements represented edge effects by both the specimen and large nearby cracks, becomes much less sensitive to the influence of specimen shape and can be attributed entirely to large cracks under or very close to the probe coil, while distributed microcracks are included in A_{material} .

In EC anisotropy measurements, besides controlling the penetration depth, changing the inspection frequency can be also used to control the ratio between the competing influences of electrical and magnetic anisotropy. Figure 10 shows a schematic representation of the mutually orthogonal electric and magnetic fields for parallel and normal probe orientation relative to the axis of the bending specimen. For EC anisotropy measurements, the material anisotropy, that was formerly given by Eq. (4) for low-frequency ACPD as equal to the resistivity anisotropy

$$A_p = \frac{\rho_{\text{parallel}} - \rho_{\text{normal}}}{(\rho_{\text{parallel}} + \rho_{\text{normal}})/2}, \quad (6)$$

should be rewritten to account for the role magnetic anisotropy

$$A_{\mu} = \frac{\mu_{\text{parallel}} - \mu_{\text{normal}}}{(\mu_{\text{parallel}} + \mu_{\text{normal}}) / 2} \quad (7)$$

as well. Combining these two effects yields the material anisotropy as the difference of these two effects

$$A_{\text{EC}} = M_{\rho} A_{\rho} - M_{\mu} A_{\mu}, \quad (8)$$

where it was exploited that in the absence of large cracks A_{shape} is negligible. The reason for the opposite signs of the two material effects is illustrated in Figure 10 that shows a schematic representation of the mutually orthogonal electric and magnetic fields for parallel and normal probe orientation relative to the axis of the bending specimen. Since both anisotropy factors are defined as the normalized difference between the corresponding parallel and normal parameters, the combined effect measured by A_{material} has to take into account that when the directional EC probe coil is oriented so that the induced eddy current is dominantly parallel with the axial direction, the magnetic field is normal to it [9]. The choice of defining the probe orientation based on the dominant eddy current direction is somewhat arbitrary, but taken so that the results are consistent with the previously introduced convention for ACPD inspection. It should be pointed out that the single gauge factor M previously introduced in Eq. (3) must be replaced with two different gauge factors, M_{ρ} and M_{μ} , to account for the different frequency-dependence of eddy current sensitivity to electrical resistivity/conductivity and magnetic permeability changes. At the same time, controlling the inspection frequency allows not only adjusting the penetration depth of EC anisotropy measurements, but also adjusting the relative strength of the two material effects, which will be demonstrated in Section 3.2.

3.1 EC Measurement Procedure

EC anisotropy measurements were made at two different inspection frequencies, namely 30 kHz and 500 kHz. In both cases a Nortec 2000D eddy current instrument was used. This instrument allows dual-frequency operation that could be exploited in the future for increasing both the sensitivity and selectivity of this method. However, such optimization was beyond the scope of the limited current effort and was left for follow-up projects. At 30 kHz operational frequency, the directional EC measurements were made using a UniWest US-1387 racetrack probe. At 500 kHz operational frequency, similar measurements were conducted using a UniWest US-1368

racetrack probe. In both cases the horizontal and vertical gains were set to 70 dB. Following routine procedures used in eddy current conductivity measurements, the phase angles were chosen so that the lift-off curves became essentially horizontal. Then the inevitable lift-off variations can be readily suppressed by measuring only the vertical voltage on the probe coil, a technique often referred to as the “vertical voltage” technique. It should be also pointed out that the phase angle was used to rotate the complex impedance plane so that decreasing lift off distance produced an increasing horizontal voltage. When this convention is used, increasing vertical voltage corresponds to increasing resistivity, i.e., decreasing conductivity, while decreasing vertical voltage corresponds to decreasing resistivity, i.e., increasing conductivity.

The instrument was nulled as necessary to assure that the readings were not saturated due to large conductivity and/or permeability variations. Because parallel and normal readings were always taken subsequently without re-nulling the instrument in between, the arbitrary nature of baseline subtraction caused by nulling the instrument affected only individual readings, but not the measured anisotropy that was defined simply as the difference between the vertical voltages measured at parallel and normal orientations of the race-track probe coil

$$A_{EC} \propto \Delta V = V_{\text{parallel}} - V_{\text{normal}}. \quad (9)$$

This simplistic anisotropy measurement procedure lacked any effort to calibrate the EC technique for absolute anisotropy measurements. The development of such a calibration procedure was beyond the scope of the limited current effort focused on establishing only the potential of feasibility of detection and quantitative characterization of precursors of fatigue crack initiation by EC anisotropy measurements, and addressing the issue of absolute calibration was also left for future projects. In the following section, EC anisotropy results will be reported in terms A_{EC} whose physical unit is volt. However, these values also depend on the level of the driving current, the applied gain setting (70 dB), and various properties of the probe coil, therefore the unit will be indicated as arbitrary or [a. u.]. Normalization to the intact value of A_{EC} was initially considered but ultimately rejected because it would have hidden the often negative sign of the measured anisotropy.

3.2 EC Measurement Results

Figure 11 shows the EC anisotropy measured at 30 kHz, where the standard penetration depth is only $\delta \approx 0.18$ mm, as a function of the number of fatigue cycles in thirty-two uncracked specimens. Like before, two sets of data are presented. Open red and blue circles represent anisotropy values spatially averaged over locations 3-8 and 5-8, respectively, for four “single” specimens at each fatigue level. In addition, solid circles of the same color indicate the ensemble average for each group of four singles tested at the same stress level (see comments in Section 2.2 concerning three specimens ran at stress levels below $\tau = 88$ ksi for $N = 2 \times 10^6$ cycles). Finally, solid lines are trend lines intended to schematically illustrate overall trends in the data. Both shorter (5-8) and longer (3-8) spatial averages start with negative baseline values in the intact specimens and show decreasing trends with increasing cycle number towards negative values of higher magnitude. These trends are consistent with the ACPD resistance anisotropy trends obtained at 4 Hz which showed that the resistivity anisotropy caused by fatigue damage is negative and its magnitude increases with increasing number of fatigue cycles.

In order to illustrate how things change at higher inspection frequency, Figure 12 shows the EC anisotropy measured at 500 kHz, where the standard penetration depth is only $\delta \approx 0.043$ mm, as a function of the number of fatigue cycles in thirty-two uncracked specimens. Although the further decreasing penetration depth itself should not change the qualitative trend observed at 30 kHz inspection frequency, the changing balance between the competing electrical resistivity and magnetic permeability anisotropies represented by Eq. (8) does that. The EC anisotropy is still negative in both intact and damaged specimens, although the magnitudes are different partly because of the different balance between A_p and A_μ and partly because the previously mentioned lack of absolute calibration. What is more interesting is that at 500 kHz the eddy current anisotropy A_{EC} increases rather than decreases with increasing fatigue damage, which cannot be attributed to the lack of absolute calibration and is likely to be entirely due the different balance between electrical resistivity and magnetic permeability anisotropies. It should be noted that, like in all other tests, the majority of the observed anisotropy change occurs in the initial phase of fatigue cycling. It is also noteworthy that, in comparison to the previously presented ACPD resistance anisotropy obtained at 4 Hz and the EC anisotropy obtained at 30 kHz, the EC anisotropy obtained at 500 kHz changes more and the scatter of the data, caused partly by

measurement uncertainties and partly by specimen-to-specimen variations, is relatively smaller with respect to the overall change of anisotropy with increasing fatigue damage.

It is also interesting to look at the minor EC anisotropy variations exhibited by the four specimens (6C, 29C, 31C and 36C) that were ran up to $N = 2 \times 10^6$ cycles at various stress levels between 80 and 88 ksi peak stress levels. Figure 13 shows the EC anisotropy measured at 500 kHz as a function of peak stress level for these specimens (the same data was also presented in Figure 10). Of course, four specimens are far from sufficient for drawing reliable conclusions. Only at 84 ksi did we have two nominally identical specimens to estimate the specimen-to-specimen variations, and it was very substantial, which is certainly expected in such an advanced stage of fatigue damage accumulation. Still, it is comforting that there is statistically significant increase in the measured EC anisotropy, especially in the data representing more extensive spatial averaging over locations 3-8. This data indicates that, after further enhancement of the EC anisotropy measurements method, this issue should be revisited using a larger set of specimens to confirm or refute this tentative observation.

4. Magnetic permeability (MP) Measurements

While room temperature electrical resistivity/conductivity measurements exhibit inherently low sensitivity to precursors of high-cycle fatigue failure and therefore require special inspection techniques, such as directional anisotropy measurements, to suppress spurious variations, magnetic permeability measurements often exhibit sufficient sensitivity to such damage accumulation even in their simplest nondirectional form. At the same time, nondirectional near-surface magnetic permeability measurements can be easily conducted by portable hand-held instruments that are widely used in the industry for equivalent ferrite content (EFC or %Fe) measurements. Therefore, nondirectional magnetic permeability measurements were also included in this project so that the role of magnetoelastic effects and ferromagnetic phase transformation [12] could be assessed.

4.1 MP Measurement Procedure

An MP30E-S Fischer Technology Feritscope was used to measure the EFC of the bending specimens [13]. The operation of this instrument is based on low-frequency (1.8 kHz) dynamic magnetic permeability measurement. The Feritscope was calibrated using reference blocks of

11.8 %Fe and 31.0 %Fe values. The EFC reading can be empirically related to the relative magnetic permeability μ_r of strongly paramagnetic and ferromagnetic steels using a quadratic regression polynomial $\mu_r \approx 1 + 0.06 \times \%Fe + 0.0194 \times \%Fe^2$ based on experimental data published by Yin *et al.* [14]. This is a relatively easy and fast measurement that is well suited for the purposes of field tests. Fifty readings were taken at the same ten locations along the axes of the specimens that were used for anisotropy measurements to increase the reliability and accuracy of the collected data by averaging.

4.2 MP Measurement Results

Figure 14 shows the measured magnetic permeability plotted as a function of the number of fatigue cycles in thirty-two uncracked specimens. Since magnetic permeability readings are inherently highly variable but insensitive to shape effects of the large bending specimens used in this study, all measurements taken at the ten preselected locations were averaged to yield a representative value for each single specimen as shown by open red circles. Solid circles represent the ensemble average for each group of four singles tested at the same stress level (see earlier comments for the group loaded to $N = 2 \times 10^6$ cycles). Finally, the solid line is intended to illustrate schematically the overall trend of the data. These results indicate that PM measurements show similar trends to anisotropy measurements with most of the change due to fatigue damage occurring early on in the fatigue life of the material followed by a weaker effect at the highest number of cycles.

In spite of the demonstrated sensitivity on nondirectional PM measurements to fatigue damage caused by bending stresses in these specimens, the selectivity of this very simple technique to fatigue damage is highly questionable since it does not have a baseline compensation mechanism similar to anisotropy measurements that could suppress common mode, i.e., nondirectional, variations present in the parallel and normal parameters. Still, it is expected that in specimens like the ones used in this study, which exhibit little specimen-to-specimen variation in their properties because of their identical alloy content, heat treatment, and machining history, MP measurements correlate well with EC anisotropy measurements. This assumption is validated by Figure 15 showing the EC anisotropy measured at 500 kHz and averaged over locations 3-8 versus the relative magnetic permeability averaged over locations 1-10 in thirty-two uncracked specimens. The solid circles represent the ensemble averages over the four specimens belonging to the same group of fatigue cycles, error bars represent the range

covered by the four specimens in the same group, and the solid line represents the best fitting linear regression line. The fairly high coefficient of prediction $R^2 = 0.82$ indicates that the observed EC anisotropy changes are, at least indirectly, correlated to the nondirectional magnetic permeability of the specimens. This was to be expected on the basis that material deformation under uniaxial stress increases the magnetic anisotropy of ferromagnetic materials while decreases their average relative permeability in the plane tangential to the surface due to magnetoelastic effects [9].

5. Discussion and Conclusions

The objective of this project was to assess the feasibility of various EMNDE techniques for early detection and characterization of high-cycle fatigue damage in martensitic steels. The presence of material damage prior to crack initiation and growth is important for service life prediction and extension of fracture critical components that might spend most of their service life in this period when fatigue damage accumulation can be assessed only through subtle crack precursors such as increasing dislocation size and density. It is widely recognized that electrical measurements are neither the most sensitive nor the most selective NDE methods available for early fatigue damage detection; that distinction belongs to nonlinear ultrasonic methods that are uniquely sensitive to early fatigue damage accumulation. However, the long-term goal of this effort is to identify the most promising candidates for field inspection of actual steam turbine blades and nonlinear ultrasonic techniques are rather difficult to adapt to field inspection. In contrast to nonlinear ultrasonic techniques, EMNDE techniques are far more adaptable to field inspection demanding simplicity, ruggedness, and portability.

Thirty-six plane bending fatigue specimens representing various levels of high-cycle fatigue exposure were provided by EPRI for this study. First, the specimens were tested using a directional ACPD technique at 4 Hz. It was found that the measurements were strongly influenced by a positive geometrical anisotropy A_{shape} related to the shape of the specimen and to a much weaker degree by the also positive intrinsic anisotropy A_{intact} of the intact, i.e., damage-free, material. In comparison, the damage-induced anisotropy A_{damage} due to fatigue cycling was negative and its magnitude increased with the number of fatigue cycles. However, the overall magnitude of A_{damage} was found to be only about 1%, a measurable level after spatial averaging over the center line of the gauge section followed by ensemble averaging over the four

specimens belonging to the same group of fatigue cycles, but insufficient for classifying individual specimens, let alone locating danger spots of excessive fatigue damage accumulation that might be sites of future fatigue crack initiation.

In order to achieve higher near-surface sensitivity to damage-induced anisotropy in the high-cycle fatigue specimens provided for this project by EPRI, directional EC techniques were also investigated at 30 kHz and 500 kHz. These measurements were found to be much less sensitive to edge effects than low-frequency ACPD measurements and offered better sensitivity to bending fatigue because of their much smaller penetration depth controlled by the inspection frequency. In addition, EC anisotropy is a combination of resistivity and permeability effects that makes it possible to optimize the sensitivity and selectivity of the inspection technique. At 30 kHz, the baseline anisotropy of the intact specimens was negative and showed a decreasing trend with increasing cycle number towards negative values of higher magnitude. This trend was similar to what was expected from ACPD measurement of damage induced resistivity anisotropy, but the effect was easier to detect partly because the suppressed geometrical anisotropy associated with the shape of the specimens and partly because of the significantly reduced penetration depth $\delta \approx 0.18$ mm. At 500 kHz where the penetration depth was only $\delta \approx 0.043$ mm, the baseline anisotropy of the intact specimens was still negative but showed an increasing trend with increasing cycle number towards negative values of smaller magnitude. This trend indicated a different balance between the electrical resistivity and magnetic permeability anisotropies at 500 kHz and at 30 kHz. More importantly, the EC anisotropy obtained at 500 kHz changed more and the scatter of the data, caused partly by measurement uncertainties and partly by specimen-to-specimen variations, was relatively smaller with respect to the overall change of anisotropy with increasing fatigue damage, than at 30 kHz.

In addition, nondirectional magnetic measurements were conducted on the same specimens at 1.8 kHz to determine whether the magnetic permeability (MP) of the material was affected by fatigue cycling. Nondirectional near-surface magnetic permeability measurements can be easily conducted by portable hand-held instruments that are widely used in the industry for equivalent ferrite content measurements, but with minor adjustments of the eddy current inspection procedure average permeability measurements could be also conducted by the instrumentation and probe coil used for EC anisotropy measurements. The obtained results indicated that PM changes exhibit similar trends to EC anisotropy changes with most of the change due to fatigue damage occurring early on in the fatigue life of the material followed by a much weaker effect at

the highest number of cycles. It was found that the EC anisotropy measured at 500 kHz correlated reasonably well with the measured relative magnetic permeability changes with a coefficient of prediction of $R^2 = 0.82$. Although this correlation was to be expected on the basis of magnetoelastic effects, its experimental validation in this project might lead to further improvements towards an optimized EMNDE technique for quantitative assessment of early fatigue damage in martensitic steels.

Generally, the overall magnitude of the measured damage-induced EM anisotropy was found to be measurable after spatial averaging over the center line of the gauge section of the specimens followed by ensemble averaging over the four specimens belonging to the same group of fatigue cycles, but it was insufficient for classifying individual specimens let alone locating danger spots of excessive fatigue damage accumulation that might be sites of future fatigue crack initiation. However, it is expected that in the future both the sensitivity and selectivity of this method can be increased using dual-frequency EC inspection. However, such optimization was beyond the scope of the current effort and was left for future follow-up projects.

6. References

- [1] Detection of Early Stage High-Cycle Fatigue Damage in Martensitic Stainless Steels for Steam Turbine Blades, EPRI Solicitation (2019).
- [2] M. Blodgett and P. B. Nagy, “Anisotropic grain noise in eddy current inspection of noncubic polycrystalline metals,” *Appl. Phys. Lett.* **72**, 1045-1047 (1998).
- [3] F. Yu and P. B. Nagy, “Dynamic piezoresistivity calibration for eddy current nondestructive residual stress measurements,” *J. Nondestr. Eval.* **24**, 143-152 (2005).
- [4] E. Madhi and P. B. Nagy, “Sensitivity analysis of a directional potential drop sensor for creep monitoring,” *NDT&E Int.* **44**, 708–717 (2011).
- [5] P. B. Nagy, “Electromagnetic Nondestructive Evaluation,” in *Ultrasonic and Electromagnetic NDE for Structure and Material Characterization* (CRC Press, Boca Raton, 2012), Chapter 3, pp. 169-248.
- [6] P. B. Nagy, G. Sposito and P. Cawley, “NDE methods for monitoring fatigue and thermal embrittlement in austenitic and ferritic steel nuclear reactor plant components,” NPCT SART3 Project Report (2008).
- [7] P. B. Nagy, J. Qu, and L. J. Jacobs, “Nonlinear Ultrasonics,” in *ASM Handbook, Vol. 17: Nondestructive Evaluation and Quality Control* (ASM International, Materials Park, 2017) Sect. 4I.
- [8] J. Corcoran and P. B. Nagy, “Compensation of the skin effect in low-frequency potential drop measurements,” *J. Nondestr. Eval.* **35**, 58 (2016).
- [9] J. Corcoran and P. B. Nagy, “Magnetic stress monitoring using a directional potential drop technique,” *J. Nondestr. Eval.* **37**, 60 (2018).
- [10] S. Prajapati, P. B. Nagy, and P. Cawley, “Potential drop detection of creep damage in the vicinity of welds,” *NDT&E Int.* **47**, 56-65 (2012).
- [11] M. Blodgett, W. Hassan, and P. B. Nagy, “Theoretical and experimental investigations of the lateral resolution of eddy current imaging,” *Mat. Eval.* **58**, 647-654 (2000).
- [12] D. Kalkhof, M. Grosse, M. Niffenegger and H. J. Leber, “Monitoring fatigue degradation in austenitic stainless steels,” *Fatigue Fract. Eng. Mater. Struct.* **27**, 595 (2004).
- [13] P. Neumaier, “On-site eddy current measurement of ferrite content in austenitic and duplex steel components,” *Mater. Eval.* **48**, 1065 (1990).
- [14] W. Yin, A. J. Peyton, M. Strangwood, and C. L. Davis, “Exploring the relationship between ferrite fraction and morphology and the electromagnetic properties of steel,” *J. Mater. Sci.* **42**, 6854 (2007).

7. Figures

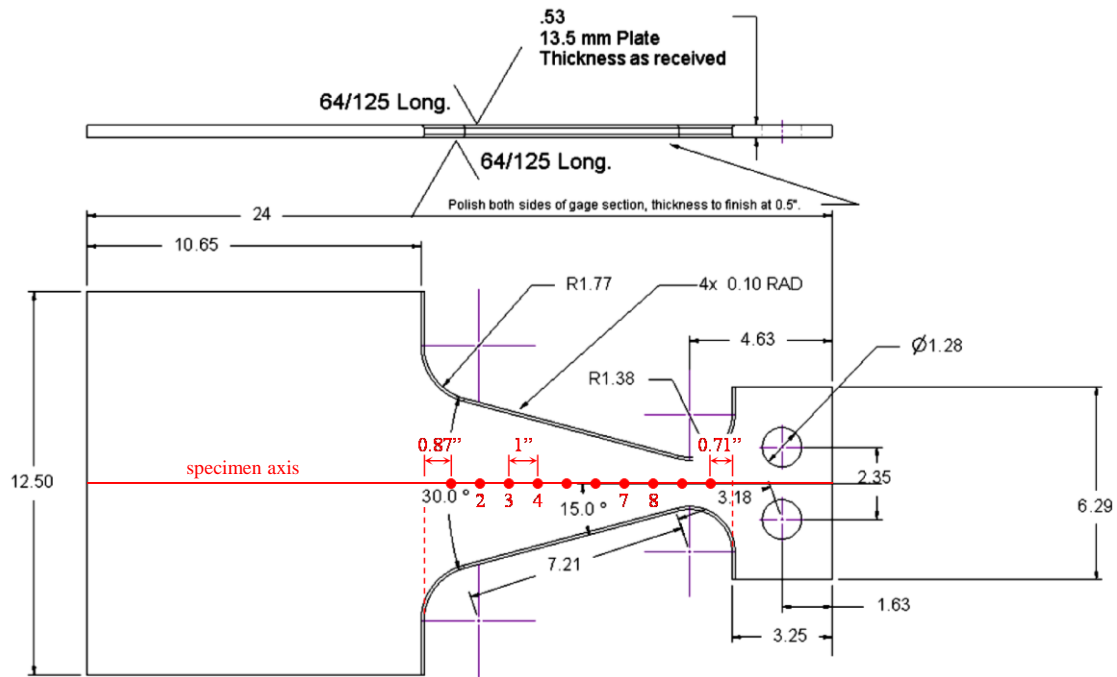


Figure 1 Geometry of the plane bending fatigue specimens provided by EPRI (dimensions in inches unless otherwise noted).

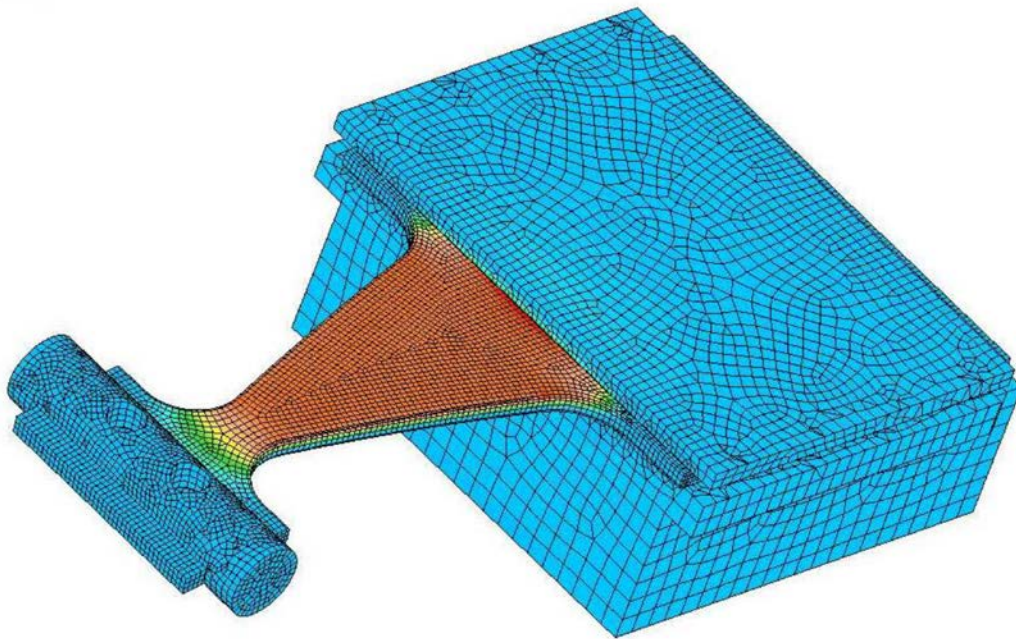


Figure 2 Simulated stress distribution on fatigue samples (from EPRI solicitation).

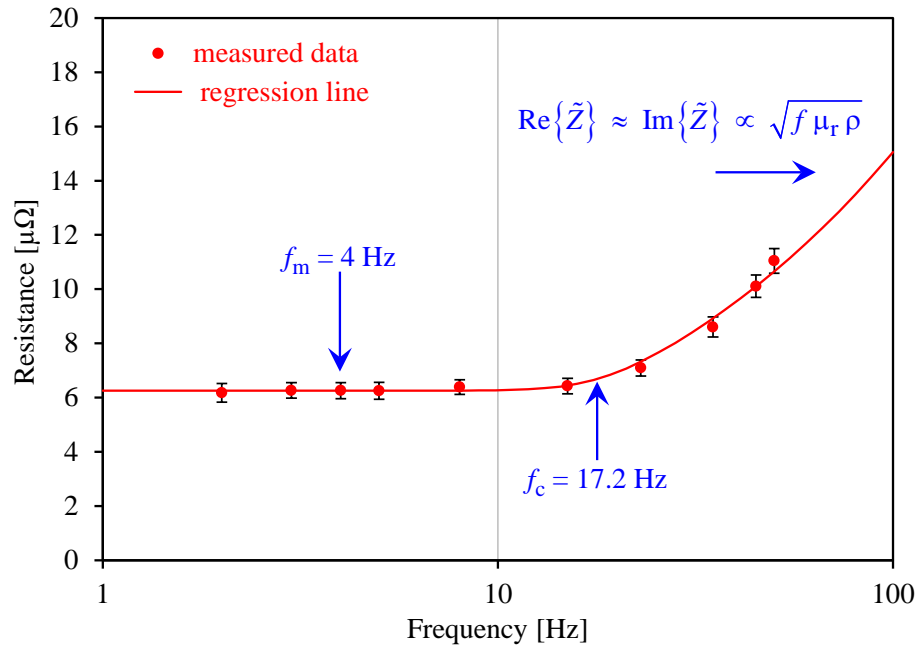


Figure 3 Electrical resistance measured by ACPD as a function of frequency.

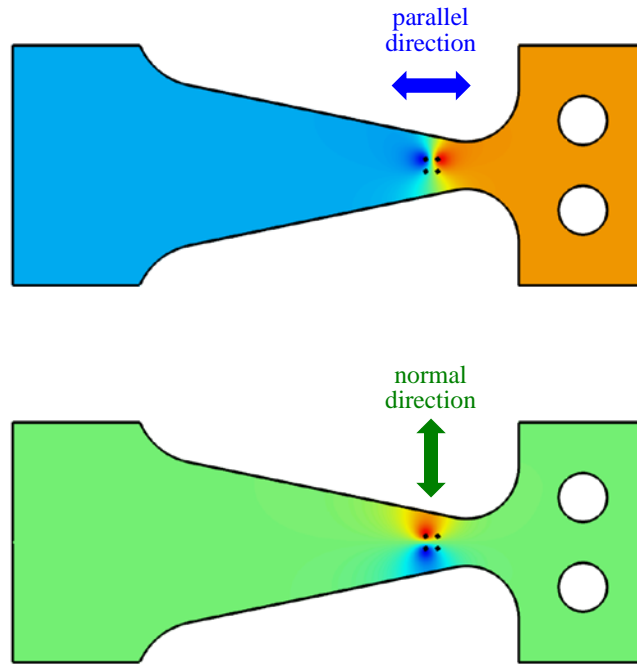


Figure 4 Electric potential distributions for parallel and normal probe orientations relative to the uniaxial stress direction in the bending specimens during loading (FE simulation).

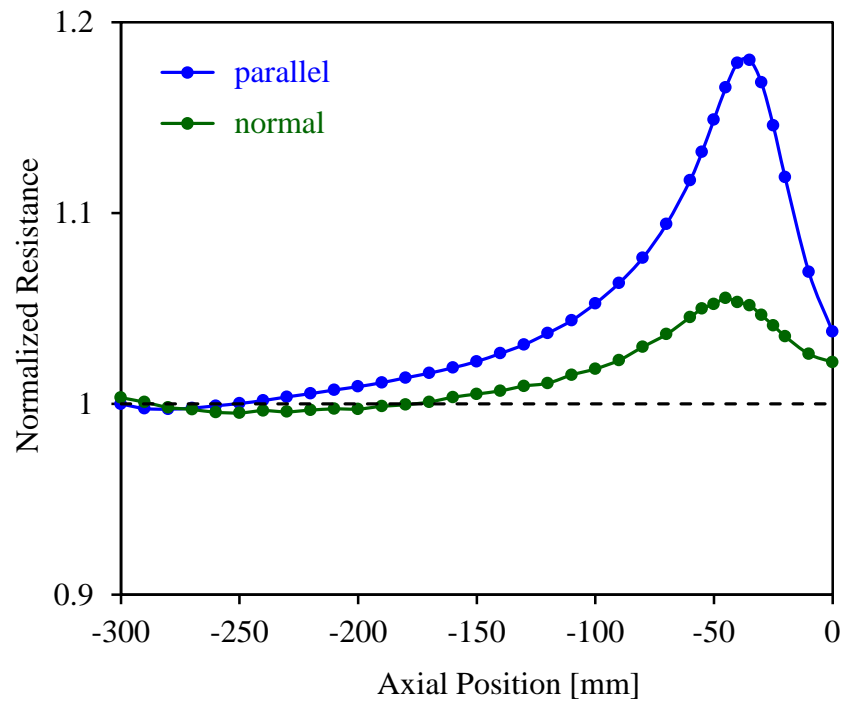


Figure 5 Parallel and normal resistances along the axis of the specimen (FE simulation).

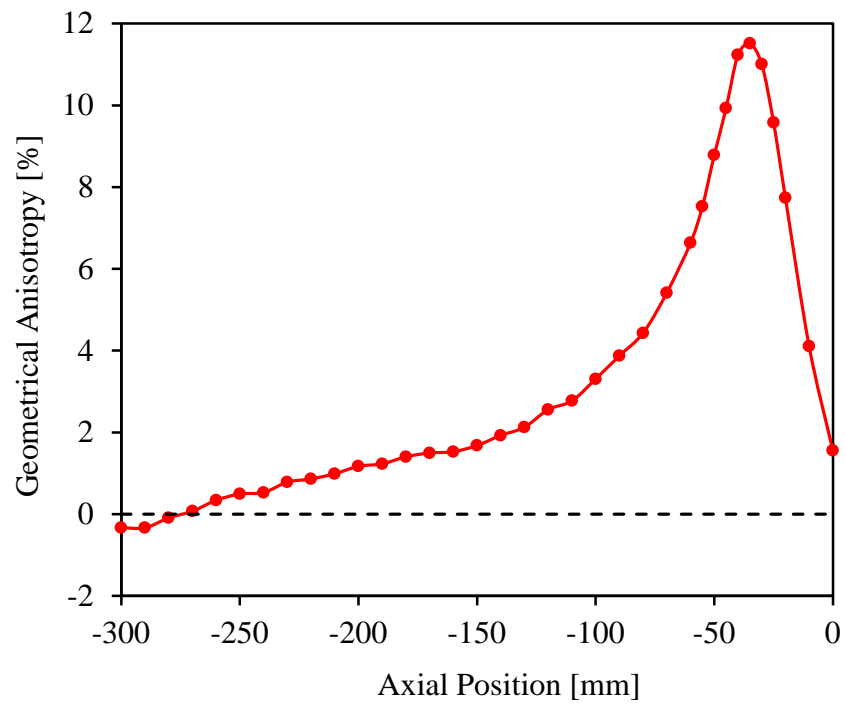


Figure 6 Geometrical anisotropy along the axis of the specimen (FE simulation).

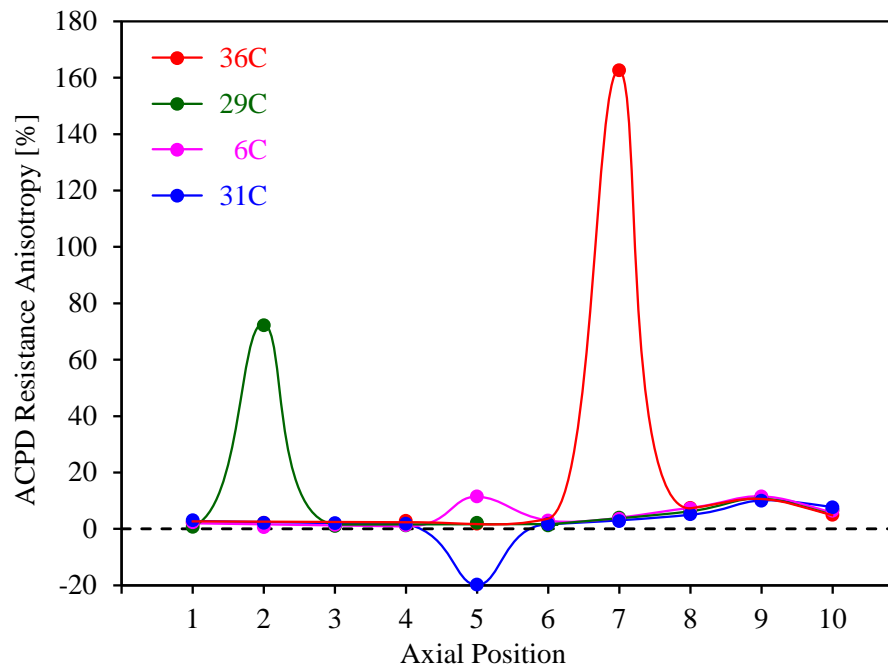


Figure 7 ACPD resistance anisotropy measured on four cracked specimens along their axes.

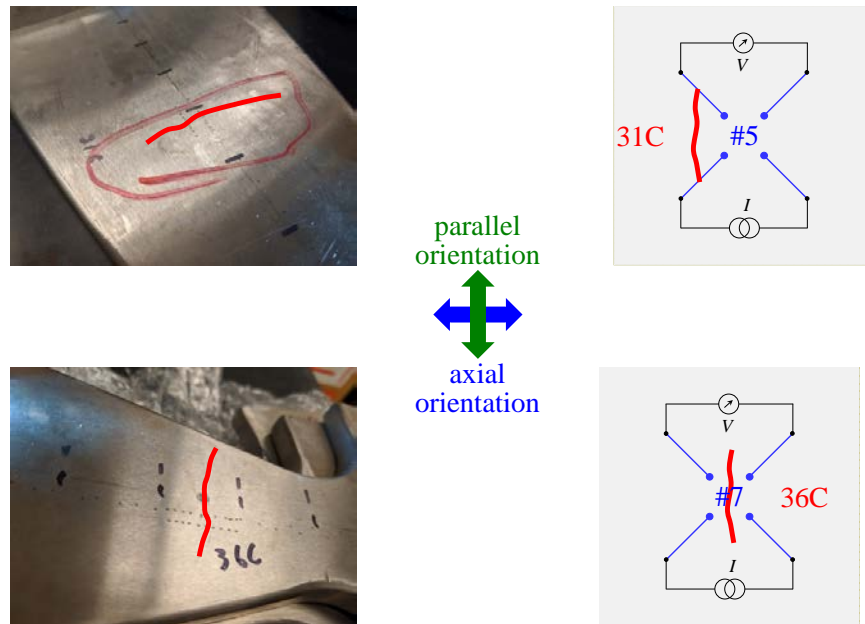


Figure 8 Optical images and schematic diagrams of cracked specimens 31C and 36C.

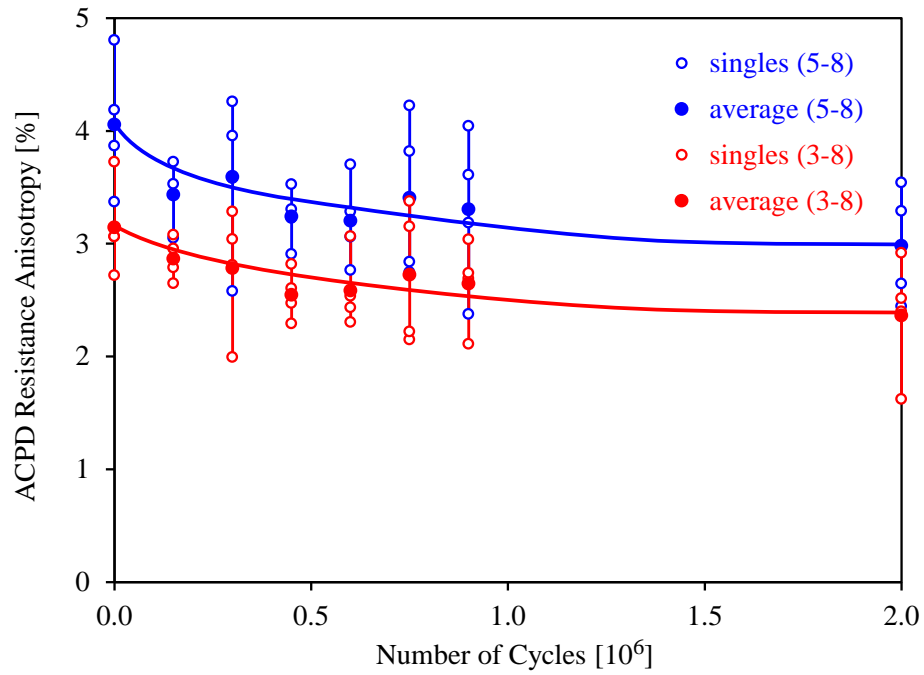


Figure 9 ACPD resistance anisotropy measured at 4 Hz as a function of the number of fatigue cycles in thirty-two uncracked specimens.

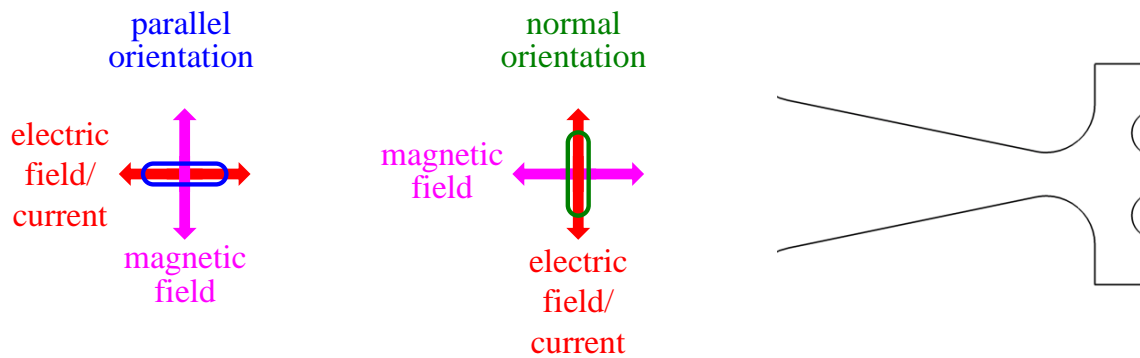


Figure 10 Schematic representation of the mutually orthogonal electric and magnetic fields for parallel and normal probe orientation relative to the axis of the bending specimen.

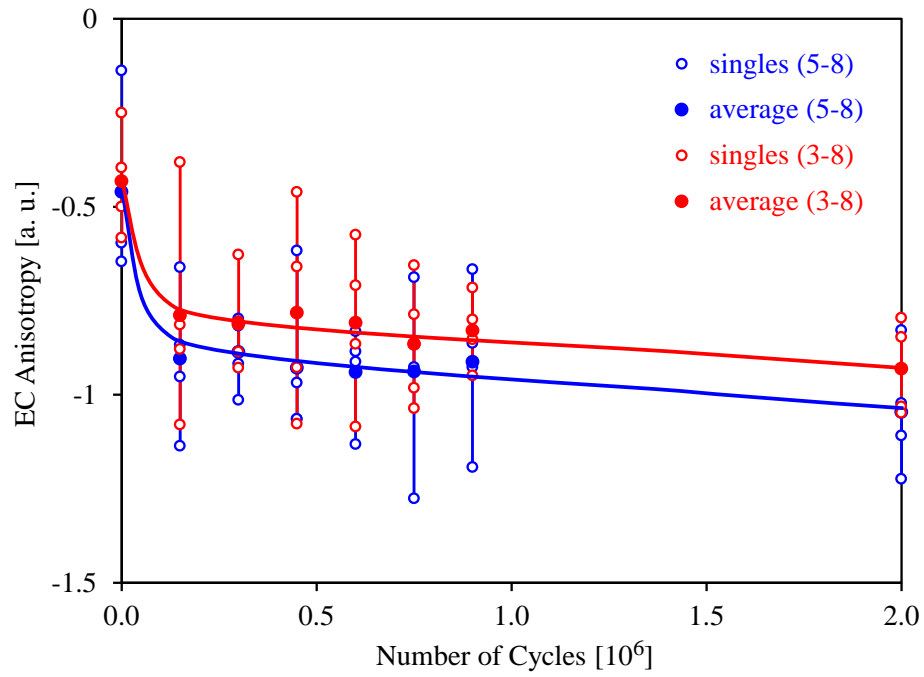


Figure 11 EC anisotropy measured at 30 kHz as a function of the number of fatigue cycles in thirty-two uncracked specimens.

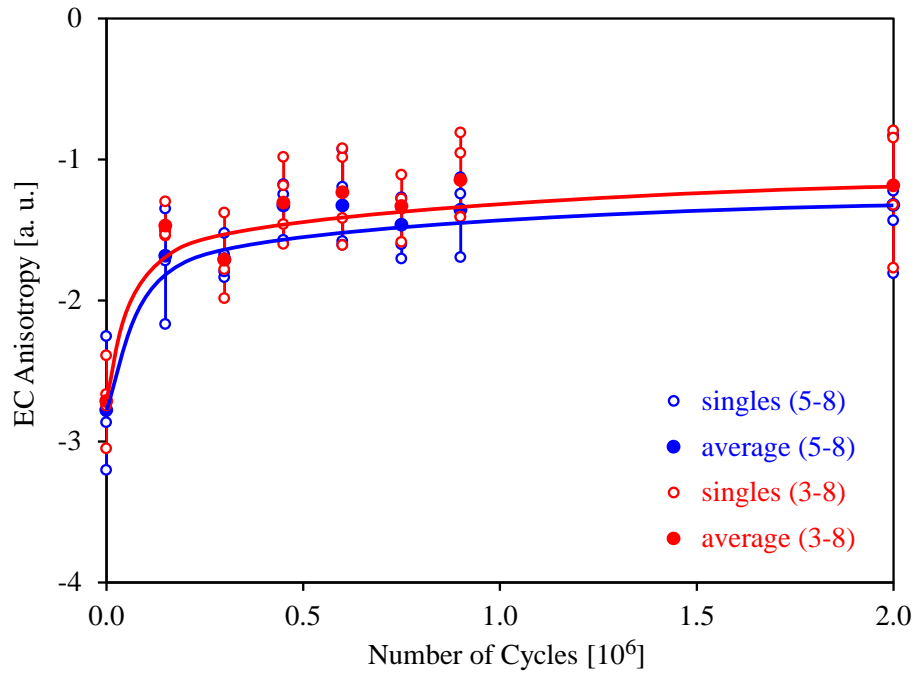


Figure 12 EC anisotropy measured at 500 kHz as a function of the number of fatigue cycles in thirty-two uncracked specimens.

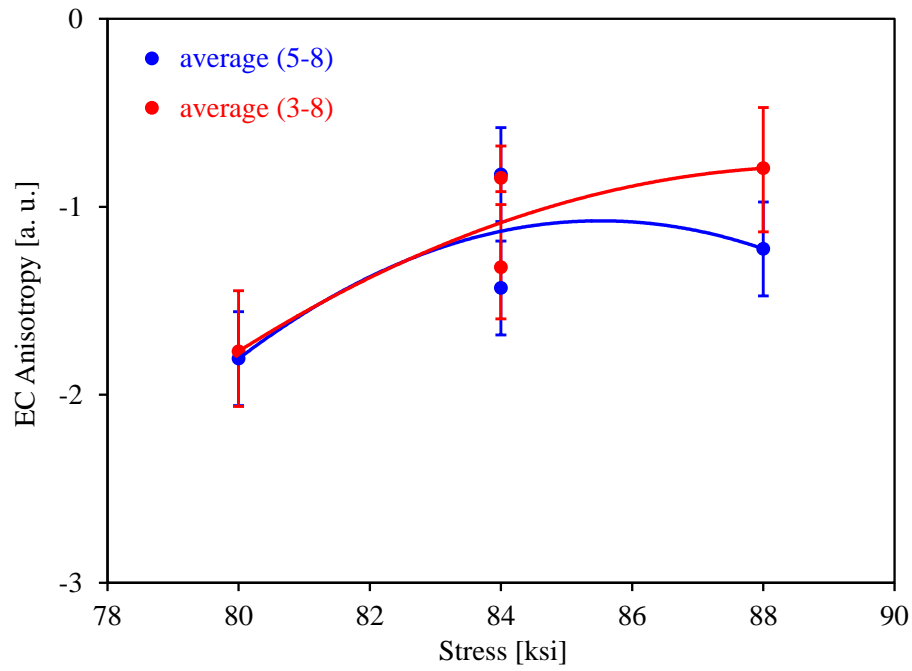


Figure 13 EC anisotropy measured at 500 kHz as a function of peak stress level for the four specimens ran up to $N = 2 \times 10^6$ cycles at various stress levels.

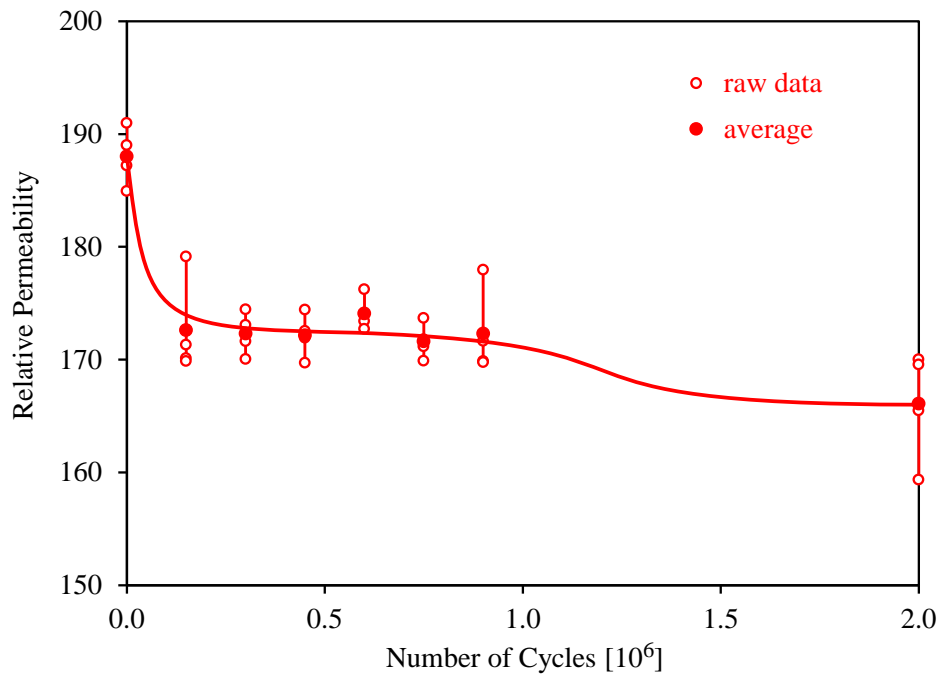


Figure 14 Magnetic permeability plotted as a function of the number of fatigue cycles in thirty-two uncracked specimens.

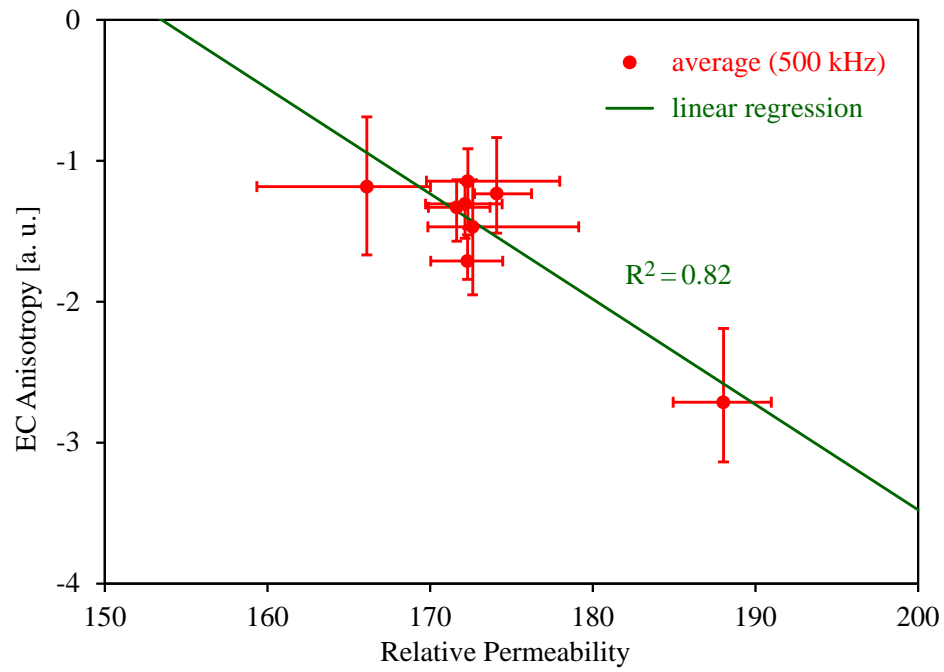


Figure 15 EC anisotropy versus relative magnetic permeability in thirty-two uncracked specimens.